

## UC Irvine

### UC Irvine Previously Published Works

**Title**

Depth-dependent redox behavior of  $\text{LiNi}_{0.6}\text{Mn}_{0.2}\text{Co}_{0.2}\text{O}_2$

**Permalink**

<https://escholarship.org/uc/item/01m1g35g>

**Journal**

Journal of the Electrochemical Society, 165(3)

**ISSN**

0013-4651

**Authors**

Tian, C  
Nordlund, D  
Xin, HL  
et al.

**Publication Date**

2018

**DOI**

10.1149/2.1021803jes]

Peer reviewed

# Depth-Dependent Redox Behavior of $\text{LiNi}_{0.6}\text{Mn}_{0.2}\text{Co}_{0.2}\text{O}_2$

Chixia Tian,<sup>1</sup> Dennis Nordlund,<sup>2</sup> Huolin L. Xin,<sup>3</sup> Yahong Xu,<sup>2,4</sup> Yijin Liu,<sup>2</sup> Dimosthenis Sokaras,<sup>2</sup> Feng Lin,<sup>5</sup> and Marca M. Doeff<sup>1\*</sup>

1. Energy Storage & Distributed Resources Division, Lawrence Berkeley National Laboratory, Berkeley, California 94720, USA.

2. Stanford Synchrotron Radiation Lightsource, SLAC National Accelerator Laboratory, Menlo Park, California 94025, USA.

3. Center for Functional Nanomaterials, Brookhaven National Laboratory, Upton, New York 11973, USA.

4. College of Mechanical Engineering, Donghua University, Shanghai 200051, China

5. Department of Chemistry, Virginia Tech, Blacksburg, Virginia 24061, USA.

\* corresponding author: e-mail: [mmdoeff@lbl.gov](mailto:mmdoeff@lbl.gov)

**Abstract**

24 Nickel-rich layered materials are emerging as cathodes of choice for next-  
25 generation high energy density lithium ion batteries intended for electric vehicles. This  
26 is because of their higher practical capacities compared to compositions with lower Ni  
27 content, as well as the potential for lower raw materials cost. The higher practical  
28 capacity of these materials comes at the expense of shorter cycle life, however, due to  
29 undesirable structure and chemical transformations, especially at particle surfaces. To  
30 understand these changes more fully, the charge compensation mechanism and bulk  
31 and surface structural changes of  $\text{LiNi}_{0.6}\text{Mn}_{0.2}\text{Co}_{0.2}\text{O}_2$  were probed using synchrotron  
32 techniques and electron energy loss spectroscopy in this study. In the bulk, both the  
33 crystal and electronic structure changes are reversible upon cycling to high voltages,  
34 whereas particle surfaces undergo significant reduction and structural reconstruction.  
35 While Ni is the major contributor to charge compensation, Co and O (through transition  
36 metal-oxygen hybridization) are also redox active. An important finding from depth-  
37 dependent transition metal L-edge and O K-edge X-ray spectroscopy is that oxygen  
38 redox activity exhibits depth-dependent characteristics. This likely drives the structural  
39 and chemical transformations observed at particle surfaces in Ni-rich materials.

40

41

42 The need for lithium-ion batteries with higher energy density and lower cost than  
43 currently available, particularly for transport applications, has led to intensified interest in  
44 Ni-rich NMC ( $\text{LiNi}_x\text{Mn}_y\text{Co}_z\text{O}_2$ ;  $x+y+z\approx 1$ , where  $x>y$ ) cathode materials.<sup>1-5</sup> These  
45 materials deliver higher practical capacities in a typically used voltage range than NMCs  
46 with lower Ni content (e.g.,  $\text{LiNi}_{1/3}\text{Mn}_{1/3}\text{Co}_{1/3}\text{O}_2$  or NMC-333), and most formulations  
47 contain less of the expensive Co component, reducing raw material costs. The increase in  
48 practical capacity roughly scales with the Ni content, but comes at the expense of cycle  
49 life and thermal stability at high states-of-charge (SOC).<sup>6</sup>

50 To circumvent these problems, several different strategies have been utilized to  
51 improve cycling, particularly to higher potentials. These include partial substitution with  
52  $\text{Ti}^{7-9}$  or  $\text{Zr}$ ,<sup>10</sup> engineering the micro- or nano-structure to reduce surface Ni content using  
53 metal segregation,<sup>11</sup> surface pillared structures,<sup>12</sup> and concentration gradients,<sup>13</sup> coating  
54 particle surfaces,<sup>14</sup> and development of electrolyte additives.<sup>15,16</sup> While all of these  
55 approaches have resulted in improvements, further understanding of the factors that lead  
56 to capacity fading is clearly needed in order to meet the stringent performance  
57 requirements of traction applications.

58 The formation of a resistive cathode/electrolyte interphase (CEI), such as an  
59 electrolyte decomposition layer, has been observed during cycling of  $\text{LiNi}_{0.4}\text{Mn}_{0.4}\text{Co}_{0.2}\text{O}_2$   
60 (NMC-442) electrodes, particularly when high voltage limits were used.<sup>17</sup> This leads to  
61 cell impedance rise and an effective loss of capacity. In addition, rock salt or mixed rock  
62 salt/spinel phases on particle surfaces have been detected under various cycling or storage  
63 conditions for NMC-442,<sup>18</sup>  $\text{LiNi}_{0.5}\text{Mn}_{0.3}\text{Co}_{0.2}\text{O}_2$  (NMC-532),<sup>19</sup> and  $\text{LiNi}_{0.8}\text{Mn}_{0.1}\text{Co}_{0.1}\text{O}_2$   
64 (NMC-811).<sup>20</sup> In the study of NMC-532, it was found that surface reconstruction to a

65 rock salt phase dominates when high voltage (4.8V) cutoffs are used due to oxygen loss  
66 under the highly oxidizing conditions, while spinel forms under milder cycling  
67 conditions. In contrast, predominantly rock salt phases, rather than spinel, were observed  
68 on NMC-442 particle surfaces even when cells were cycled to conservative limits, or  
69 during storage without electrochemical operation, although reconstruction was more  
70 severe during high voltage cycling. In the case of NMC-811, no obvious bulk crystal  
71 structure changes were observed after extensive cycling (200 cycles) and parasitic  
72 reactions between the highly delithiated cathode surface and electrolyte were suggested  
73 as the major contributor to capacity fading.<sup>15,20</sup> However, for the parent compound  
74  $\text{LiNiO}_2$ , it has been found that degradation of the bulk crystal structure contributes to  
75 capacity fading.<sup>21</sup> Two phase conversions (H1 to H2, and H2 to H3) occur during  
76 delithiation/lithiation of  $\text{LiNiO}_2$ , with H3 formation occurring at high SOC during  
77 cycling. In contrast, this phase is rarely encountered during cycling of NMCs, as it occurs  
78 outside the normal operating voltage range.<sup>22</sup> The degradation of cycling performance for  
79  $\text{LiNiO}_2$  is associated with the loss of the H3 phase during long term cycling. These  
80 observations suggest that a systematic investigation of surface and bulk phenomena  
81 involved in cycling Ni-rich NMCs is needed to determine the driving factors for capacity  
82 fading.

83 In this work, we present a comprehensive investigation of the crystal and  
84 electronic structure changes of  $\text{LiNi}_{0.6}\text{Mn}_{0.2}\text{Co}_{0.2}\text{O}_2$  (NMC-622), both at the surface and  
85 in the bulk. Towards this end, we employed a combination of synchrotron *in-operando*  
86 X-ray diffraction (XRD), soft X-ray absorption spectroscopy (soft XAS) with different  
87 detection modes to probe different depth, annular dark-field scanning transmission

88 electron microscopy (ADF-STEM) and electron energy loss spectroscopy (EELS). By  
89 probing the electronic structure of both the transition metal ions and lattice oxygen during  
90 the first cycle and long term cycling, we were able to correlate the surface reconstruction  
91 to highly reactive surface oxygen. These results suggest that surface treatments may be  
92 the best approach for improving cycle life of Ni-rich NMCs by slowing down the kinetics  
93 of interfacial reactions.

## 94 **Experimental Section**

### 95 *Synthesis of $\text{LiNi}_{0.6}\text{Mn}_{0.2}\text{Co}_{0.2}\text{O}_2$*

96 NMC-622 pristine powder was synthesized by ultrasonic spray pyrolysis followed  
97 by thermal annealing. The general procedure has been reported in previous  
98 publications.<sup>11,23,24</sup> Different parameters, including precursor solution concentration,  
99 injection rate, gas carrier flow rate and spray pyrolysis temperature, were studied to  
100 optimize the synthesis conditions. For the material used in this study, the following  
101 conditions were used. A 2M aqueous solution of  $\text{LiNO}_3$  (Sigma Aldrich),  $\text{Ni}(\text{NO}_3)_2 \cdot 6\text{H}_2\text{O}$   
102 (Sigma Aldrich),  $\text{Co}(\text{NO}_3)_2 \cdot 6\text{H}_2\text{O}$  (Sigma Aldrich) and  $\text{Mn}(\text{NO}_3)_2$  (45–50 wt% solution  
103 in dilute nitric acid, Sigma Aldrich) with a molar ratio of 1.2:0.6:0.2:0.2 was prepared  
104 and transferred into a syringe pump. The solution was injected at a flow rate of 0.25  
105 ml/min and sprayed into micro-sized droplets using a 120 kHz wide spray ultrasonic  
106 atomizer, which generates droplets with an average size of 12.5  $\mu\text{m}$ . The droplets were  
107 then carried into a preheated horizontal quartz tube (700 °C) by air with a flow rate of 10  
108 liters per minute (LPM). The as-synthesized powder was then collected and further  
109 annealed in air box furnace for 4 hrs at 480 °C and 4 hrs at 850 °C, using a ramping rate  
110 of 2 °C/min.

111 *Electrode preparation and electrochemical studies*

112 A composite electrode slurry was prepared containing active material,  
113 polyvinylidene fluoride (PVdF) (Kureha Chemical Ind. Co. Limited) in N-methyl-2-  
114 pyrrolidinone (6%, wt%), and acetylene carbon black (Denka, 50% compressed), with  
115 solid matter ratios of 84:8:8 and cast onto carbon-coated aluminum current collectors  
116 (Coveris). The electrodes were then dried in a vacuum oven overnight at 120°C and cut to  
117 size. Typical active material areal loadings were 2.0–2.5 mg cm<sup>-2</sup>. 2032 coin cells using  
118 these cathodes, Li metal as the negative electrode, Celgard 2400 as the separator, and 1 M  
119 LiPF<sub>6</sub> solution in 1:1 v/v ethylene carbonate/diethyl carbonate (EC-DEC, Novolyte  
120 Technologies) as the electrolytic solution were assembled in an argon-filled glove box.  
121 Cells were allowed to rest for 12 hrs before testing with a VMP3 potentiostat/galvanostat  
122 (BioLogic) system. Galvanostatic cycling was performed at C/10, where 1C is defined as  
123 the theoretical capacity of NMC-622, i.e., 276 mAh g<sup>-1</sup>, discharged or charged in one  
124 hour. For post characterization, the electrodes were collected from disassembled coin  
125 cells, rinsed with dimethyl carbonate and dried in an argon-filled glove box.

126 *Materials characterization*

127 To determine phase purity, powder XRD patterns were collected using a Bruker D2  
128 Phaser diffractometer with Cu K $\alpha$  radiation. Pristine powder was dissolved in  
129 concentrated nitric acid and analyzed with an inductively coupled plasma optical  
130 emission spectrometer (ICP-OES, Perkin-Elmer Optima5400) to determine the chemical  
131 composition. Scanning electron microscopy (SEM) was performed on a JEOL JSM-  
132 7000F with a Thermo Scientific energy dispersive X-ray spectroscopy (EDS) detector.  
133 The ADF-STEM imaging was performed on a 200 keV cold-field-emission probe-

134 corrected instrument equipped with an Enfina EELS at Brookhaven National Laboratory.  
135 For soft XAS experiments, samples were mounted on an aluminum sample holder with  
136 double-sided carbon tape in an argon-filled glove box, transferred in a double-contained  
137 jar to a glove bag purged with argon connected to the XAS load-lock  
138 chamber. Measurements were conducted on the bending magnet beamline 8-2 at  
139 Stanford Synchrotron Radiation Lightsource (SSRL) using a ring current of 500 mA and  
140 a 1100 lines\*mm<sup>-1</sup> spherical grating monochromator. The monochromator was operated  
141 with 40µm entrance and exit slits, providing ~2.0×10<sup>10</sup> ph s<sup>-1</sup> at 0.4 eV resolution in a 0.1  
142 x 0.1 mm<sup>2</sup> beam spot. Data were acquired under ultrahigh vacuum (10<sup>-9</sup> Torr) in a single  
143 load at room temperature using Auger electron yield (AEY, measured by a cylindrical  
144 mirror analyzer at constant kinetic energy), total electron yield (TEY, measured by  
145 sample drain current) and Fluorescence Yield (FY, measured with an IRD AXUV-100  
146 silicon diode). All spectra were normalized by the current from a gold-evaporated fine  
147 grid positioned upstream of the main chamber. For transition metal L-edges, a linear fit  
148 background was removed and then the maximum intensities are normalized to unity. This  
149 normalization method has negligible effect for the transition metal L-edge data  
150 interpretation since the peak position (e.g., Co L-edge)/peak shape (e.g., Mn L-edge) or  
151 the relative peak intensity ratio (e.g., Ni L<sub>3</sub> high to L<sub>3</sub> low peak intensity ratio) were used  
152 to quantify the oxidation states. However, oxygen K-edge data was normalized using a  
153 different method, where a linear background fit to the pre-edge region (520 eV to 525  
154 eV) was subtracted from the spectra and the post-edge (565 eV to 580 eV) was  
155 normalized to unity. For samples that have lithium carbonate layers on the surface, a  
156 correction was applied; details are discussed in supporting information. *Operando*



157 synchrotron X-ray diffraction studies were performed at beamline 11–3 at SSRL. The  
158 coin cell components (bottom case, spacer and top cap) were pierced with 2mm holes.  
159 Kapton tape was used to cover the holes on the bottom cases and top caps. The cells were  
160 then assembled the same way as other 2032 coin cells. Aluminum tabs were attached to  
161 either sides of the coin cell and sealed in a polyester pouch. See reference<sup>25</sup> for further  
162 details. The cell was cycled at a rate of 28 mA g<sup>-1</sup> (~0.6 mA/cm<sup>2</sup>). Transmission XRD  
163 ring patterns were detected using a MAR image plate and were collected every minute.  
164 Selected patterns (every 20 mins) were plotted in this work. LaB<sub>6</sub> patterns were collected  
165 as reference data for calibration, and exposure time was only a half second for the  
166 samples to avoid any saturation. For ease of comparison, all data was converted to same  
167 pattern as the Bruker Cu K $\alpha$  ( $\lambda=1.54$  Å) format. A blank cell containing all other  
168 components except the active cathode material was also assembled and measured, as  
169 shown in Figure S1. Therefore, peaks attributable to the Kapton tape and the packing  
170 pouch bag could be identified, and a background could be subtracted.

## 171 **Results and Discussion**

### 172 *Characterization of pristine NMC-622 materials*

173 An SEM image of NMC-622 pristine powders is shown in Figure 1a. The  
174 secondary particles consist of agglomerated primary particles ranging in size from 200  
175 nm to 800 nm (Figure 1a inset) and have a spherical shape about 5 $\mu$ m to 13 $\mu$ m across in  
176 diameter (Figure 1a). The resulting NMC-622 materials are phase pure and all reflections  
177 in the XRD pattern (Figure 1b) can be indexed to the  $R\bar{3}m$  space group with the layered  
178 rhombohedral structure of  $\alpha$ -NaFeO<sub>2</sub>. The high-resolution STEM image in Figure 1c  
179 reveals the nearly ideal layered structure where almost no transition metals occupy the Li

180 channels (lithium ions are not visible in the STEM imaging). STEM-EELS analysis was  
181 performed for the particle shown in Figure 1d (red dashed arrow shows the direction of  
182 EELS scanning) and show that the oxidation states of three transition metals (i.e., Mn, Co  
183 and Ni) and oxygen remain almost unchanged from the surface to the bulk (Figure 1e).

184 We also used ensemble-averaged synchrotron soft XAS to characterize the  
185 pristine material. The beam size of  $1 \times 1 \text{ mm}^2$  characterizes millions of sub-micron sized  
186 primary particles simultaneously, complementing the STEM-EELS experiment, in which  
187 only one or a few particles can be probed. In addition to delivering ensemble-averaged  
188 information, the three different detection modes, namely AEY, TEY and FY, of  
189 synchrotron based soft XAS have the capability of probing different depths (AEY, 1-2  
190 nm; TEY,  $\sim 5$  nm; FY,  $\sim 50$ -100 nm). Soft XAS transition metal (TM) L-edge experiments  
191 directly probe the dipole allowed 2p-3d transition of transition metals, which provides  
192 unique fingerprint of their valence states and the detailed multiplet structure is also  
193 sensitive to spin and symmetry.<sup>26</sup> The spectra of transition metals are spin-orbit split into  
194 an  $L_3$ -edge ( $2p_{3/2}$ ) at lower energy and an  $L_2$ -edge ( $2p_{1/2}$ ) at higher energy. XAS L-edge  
195 spectra of Mn and Co (Figure 2a and Figure 2b) in AEY, TEY and FY modes show  
196 identical shapes and peak intensities, which suggest that the oxidation states of Mn and  
197 Co are homogeneous from the surface to the bulk. The valence states are further  
198 determined to be  $\text{Mn}^{4+}$  and  $\text{Co}^{3+}$  as expected. For the Ni L-edge spectra, about 17 eV  
199 separates the Ni  $L_3$  and the Ni  $L_2$  peaks. As shown in Figure 2c, the Ni  $L_3$  multiplet  
200 structure has the most spectral weight in two locations (peak A in the lower energy region  
201 and peak B in the higher energy region) in the  $L_3$  edge absorption band (for details of the  
202 electronic structure origin based on spin and symmetry of the Ni center, see reference 26.

203 The relative intensity ratio for peak B/peak A can be utilized as an indicator for changes  
204 of oxidation states.<sup>18,21</sup> The ratio increases as Ni is oxidized. Comparing the relative  
205 intensities of these two peaks in the different modes shows that the surface Ni (AEY and  
206 TEY in Figure 2c) is slightly reduced in comparison to the bulk. A similar phenomenon  
207 was also detected for LiNiO<sub>2</sub>,<sup>21,27</sup> which suggests that there is instability of surface Ni in  
208 nickel-rich materials before electrochemical cycling and even without any interaction  
209 with the electrolytic solution. However, the surface reduction of Ni for the NMC-622  
210 material is minimal, and the average oxidation state is still much higher than Ni<sup>2+</sup> (orange  
211 dashed line in Figure 2c represents LiNi<sub>1/3</sub>Mn<sub>1/3</sub>Co<sub>1/3</sub>O<sub>2</sub>, where all Ni cations are in the  
212 Ni<sup>2+</sup> oxidation state). The results from soft XAS are consistent with the EELS analysis,  
213 collectively demonstrating a homogeneous distribution of electronic structures for all the  
214 transition metal cations in the pristine material with minimal reduction of Ni at particle  
215 surfaces.

216 The O K-edge data is shown in Figure 2d. The O K-edge includes a higher energy  
217 region (>535 eV) associated with O 1s transitions to hybridized TM4sp-O2p states and a  
218 lower energy region (<535 eV) originating from O 1s transition to TM3d-O2p hybridized  
219 states.<sup>28</sup> The lower energy region is of most interest here. Four peaks or shoulders  
220 (labeled 1, 2, 3, and 4 in Figures 2d and 2e) can be assigned by comparison to standard  
221 samples. Red open circles depict the FY data and black open circles the TEY data for the  
222 pristine NMC-622 in Figure 2e. Peak 1 (~528.5 eV) corresponds to the Ni<sup>3+</sup> 3d-O 2p  
223 hybridized state, as is found in LiNiO<sub>2</sub> (orange curve in Figure 2e). Peak 2, which is  
224 relatively broad and centered around 530 eV, can be attributed to Mn<sup>4+</sup> 3d-O 2p  
225 hybridization, although Co<sup>3+</sup> 3d-O 2p and Ni<sup>3+</sup> 3d-O 2p may also contribute, as evidenced

226 by a comparison with  $\text{LiCoO}_2$  (brown curve) and  $\text{LiNiO}_2$  (orange curve). Peak 3  
227 ( $\sim 532\text{eV}$ ) mainly arises from the contribution of  $\text{Mn}^{4+}$  3d-O 2p (pink curve for  $\text{MnO}_2$ )  
228 although  $\text{Ni}^{2+}$  3d-O 2p (blue curve for  $\text{NiO}$ ) may also contribute. In this region, there is  
229 some overlap of TM-O signals.<sup>29–31</sup> However, while some  $\text{Ni}^{2+}$  (as well as  $\text{Ni}^{3+}$ ) is  
230 expected to be present in the pristine material, it is significant that this peak is stronger in  
231 the TEY mode than in FY mode. This is consistent with the observation in the Ni L-edge  
232 data that Ni on the surface is marginally more reduced than it is in the bulk. A sharp peak  
233 around 534 eV (peak 4 in Figure 2e) matches the green curve for pure  $\text{Li}_2\text{CO}_3$ .  $\text{Li}_2\text{CO}_3$  is  
234 frequently observed as a stable by-product on particle surfaces of nickel-rich lithium-host  
235 materials.<sup>6,21,27</sup> This peak is only observed in AEY and TEY mode (Figure 2d) and not in  
236 FY mode (Figure 2d), showing that  $\text{Li}_2\text{CO}_3$  is present on surfaces only a few nm deep.

### 237 *Changes in bulk and surface electronic structures during the initial cycle*

238 NMC electrodes are commonly cycled to 4.3V in lithium half-cells, with practical  
239 capacities rising as the Ni content is increased, although the theoretical limit of  $\sim 280$   
240 mAh/g is not attained.<sup>2,6,32</sup> Raising the charge voltage limit to 4.7V vs.  $\text{Li}^+/\text{Li}$  results in  
241 increased utilization,<sup>9</sup> but lower capacity retention upon cycling due to rising cell  
242 impedance.<sup>17,18</sup> Figure S2 shows capacity retention data for half cells containing NMC-  
243 622 cycled to various voltage limits. Because of the presence of lithium carbonate on  
244 particle surfaces, the initial cycle discharge capacity is lower than on subsequent cycles  
245 when cells are charged to 4.7V. After the second cycle to 4.7V, a maximum discharge  
246 capacity of 202 mAh/g was reached, while the cell charged to 4.3V reached its maximum  
247 capacity after 6 cycles.

248 Bulk crystal structure changes leading to microstrain,<sup>33</sup> cracking,<sup>34</sup> and  
249 disconnection<sup>35</sup> have been implicated in cycling losses of layered oxide materials.  
250 Synchrotron based *in operando* XRD offers the opportunity to capture subtle structure  
251 changes while performing electrochemistry simultaneously. Data for a Li/NMC-622 cell  
252 were collected for the initial charge and discharge processes at a rate of about C/10  
253 between 2.5 V to 4.7 V. Representative patterns are plotted as a function of cell voltage  
254 in Figure 3a. The charge-discharge profile for in situ XRD is also shown here, with the  
255 corresponding lithium content calculated from the coulometry. Note that, because of  
256 differences in the *in situ* cell configuration compared to the *ex situ* cells, the discharge  
257 capacity is somewhat lower than that found for regular cells. The NMC-622 cathode  
258 material showed behavior intermediate between that of NMC-333<sup>22</sup> and LiNiO<sub>2</sub><sup>36</sup> or  
259 LiNi<sub>0.8</sub>Co<sub>0.15</sub>Al<sub>0.05</sub>O<sub>2</sub> (NCA) in terms of the phase behavior. The H1+H2 two-phase  
260 region occurs over a narrower voltage window in NMC-333 and the H3 phase only  
261 appears at potentials above 5V vs. Li/Li<sup>+</sup>. In the case of NMC-622, two hexagonal phases  
262 (H1 and H2) co-exist between 3.83-3.9V, with the H3 phase appearing only near 5V  
263 (Figure S3). Because cells are rarely cycled to such high potentials, the capacity fading  
264 associated with the large volume change of the H2 to H3 transition in the Li<sub>x</sub>NiO<sub>2</sub>  
265 system<sup>21</sup> can be completely avoided.

266 The excellent reversibility of the NMC-622 cathode when cycled between 2.5 and  
267 4.7V in a lithium half-cell is evident from the patterns in Figure 3a. The lattice parameter  
268 and cell volume changes are shown in Figure 3b and c. As lithium ions are removed from  
269 the structure, the *c* lattice parameter initially expands while the *a* lattice parameter  
270 decreases. Above 4.2V, a dramatic contraction of the *c*-axis with slight expansions along

271 the *a*-axis and *b*-axis are observed. However, these processes are completely reversible,  
272 and the overall volume change upon delithiation to 4.7V (approximately 90% delithiated  
273 in the *in situ* cell) is only about 4%. The results indicate that the bulk crystal structure  
274 remains quite stable and reversible during redox processes, consistent with that reported  
275 in the literature.<sup>15</sup>

276 Soft XAS was used to monitor the electronic structure changes at both the surface  
277 and the bulk, as a function of SOC of the NMC-622 cathode. For these experiments,  
278 electrodes were collected from partially and fully charged or discharged half-cells and  
279 characterized *ex situ*. Data from both TEY and FY modes of the L<sub>3</sub> edges of the three  
280 transition metals are plotted in Figure 4. As shown in Figure 4a, no change is observed  
281 for Mn from the surface sensitive TEY spectra and bulk sensitive FY spectra, indicating  
282 that Mn<sup>4+</sup> remains electrochemically inactive in NMC-622 during cycling, as expected.  
283 However, there is some variation observed between the Mn FY and TEY modes for the  
284 50% and 100% charged samples. We hypothesize the small distortion is most likely due  
285 to self-absorption and saturation effects, based on the analysis in reference 37. It has been  
286 reported that inverse-partial-FY (IPFY) XAS would suppress this distortion. However,  
287 we believe the small distortion is not related to the redox activity of Mn as more  
288 significant changes for both the line shape and intensity would be expected.<sup>38</sup> In contrast,  
289 Co L<sub>3</sub>-edge XAS spectra shift to higher energy in charged and partially charged  
290 electrodes and back to lower energies in the discharged electrodes. The shifting indicates  
291 that Co is partly oxidized during charge and reduced during the discharge (Figure 4c).  
292 The behavior of Co is similar at the surface and in the bulk. The L<sub>3</sub> peak position is  
293 consistent with trivalent Co in the pristine electrode, and shifts from 780.9 eV to 781.3

294 eV at the top of charge for a total difference of 0.4 eV. In comparison,  $\text{Co}^{3+}$  to  $\text{Co}^{4+}$   
295 changes in model compounds not only involves an larger absolute energy shift but also  
296 show another peak for  $\text{Co}^{4+}$  at lower energy in the  $L_3$  region.<sup>39,40</sup> This indicates that Co in  
297 NMC-622 is not fully charged to  $\text{Co}^{4+}$  and only partially contributes to the charge  
298 compensation during lithium deintercalation and intercalation processes under these  
299 conditions.

300 The most dramatic changes occur with Ni, however, both on the surface and in the  
301 bulk (Figure 4a). As discussed earlier, the relative intensity ratios of the higher to lower  
302 energy  $L_3$  peaks track the oxidation state changes of nickel. These ratios are plotted as a  
303 function of SOCs in Figure 4d, showing that there are significant changes in the redox  
304 states of Ni upon charging and discharging, both in TEY and FY modes. Therefore, it can  
305 be concluded that redox processes involving Ni are the major contributors to charge  
306 compensation in NMC-622 during cycling. However, the surface nickel (TEY) is  
307 consistently more reduced than the bulk nickel (FY) at different SOCs, indicating that the  
308 surface activity is different from that of the bulk. Similar surface phenomena have been  
309 reported for other systems such as  $\text{LiNi}_{0.8}\text{Co}_{0.2}\text{O}_2$ <sup>41-43</sup> and  $\text{LiNiO}_2$ <sup>27</sup>.

310 Figures 5a and b shows the O K-edge data for electrodes at different SOCs. For  
311 the pristine electrode (black curve) and the 50% charged electrode (red curve), there is a  
312 peak at 534 eV in the TEY spectra, which can be assigned to the oxygen in  $\text{Li}_2\text{CO}_3$ . This  
313 peak was not observed for the same electrodes in the FY mode, indicating that the  $\text{Li}_2\text{CO}_3$   
314 layer is surface-bound and relatively thin. In the electrode charged to 4.7V, however, the  
315 O K-edge of  $\text{Li}_2\text{CO}_3$  disappeared completely due to the electrochemical decomposition of  
316  $\text{Li}_2\text{CO}_3$  at high potentials.

317 The intensity of the TM3d-O2p states in the O K-edge, originate from the  
318 O1s→O2p dipole transition into unoccupied hybridized states which has gained O2p  
319 character through the covalent interaction, where both the degree of covalency and the  
320 total number of unoccupied d-states determine the total oscillator strength.<sup>28</sup>  
321 Phenomenologically, the integrated intensity in this region (region #1 in Figures 5a and  
322 5b) will thus represent the redox activity of the oxygen, since the effective number of  
323 holes in the oxygen (through the TM-O interaction) is proportional to this area.<sup>44</sup> We note  
324 that there is an increase in the number of unoccupied states in the TM3d-O2p hybridized  
325 orbitals as a function of lithium deintercalation. This can be attributed to the greater  
326 number of d-holes and the sharing of these holes with the oxygen ligands, as well as the  
327 associated increase in covalency that further shifts hole distribution onto the ligands. In  
328 order to extract semi-quantitatively the redox activity of the oxygen, the integrated  
329 intensity in the lower energy region (<534 eV) is plotted for the samples at various SOCs  
330 (Figures 5c and d). Note that in order to compare the strength of the pre-edge relative to  
331 the ionization potential, the spectra need to be consistently normalized at higher energies,  
332 and compounds other than lattice oxygen (such as the carbonate at the surface) have been  
333 subtracted and then the spectrum re-normalized (see pristine and 50% charged in Figures  
334 5c and 5d, where the orange error bars reflect the errors in the subtraction procedure;  
335 details are discussed in the supporting information and shown in Figures S4 and S5). In  
336 addition, for the integrated sums in Figure 5d, we first performed a self-absorption  
337 correction to the FY spectra (violet error bars) in order to allow comparison of oscillator  
338 strengths at various intensities without non-linear artifacts (Figure S6). It is noted that



339 such a rigorous data processing for oxygen K-edge quantification has sometimes been  
340 neglected in the literature.

341 Comparing the data in TEY and FY modes (Figure 6), we found that the  
342 integrated intensity of TM3d-O2p hybridization peak was much higher in the FY mode in  
343 the pristine and fully discharged electrodes, indicating that the bulk in the NMC-622  
344 particles has more TM3d-O2p unoccupied states under these conditions. This is  
345 consistent with the Ni L-edge soft XAS data, where Ni has a higher oxidation state in the  
346 bulk compared to the surface. Secondly, we observed that the change of the integrated  
347 intensity was more dramatic in the TEY mode, which strongly suggests that the surface  
348 region of the NMC-622 material underwent more dynamic changes of hole states in the  
349 TM3d-O2p hybridization. The relative integrated intensity change is only ~18% in the  
350 bulk (FY) but is ~33% (TEY) on the surface going from the pristine state to that in the  
351 electrode charged to 4.7 V. Interference from the  $\text{Li}_2\text{CO}_3$  signal required special  
352 normalization procedures for the data obtained from the pristine and partially charged  
353 electrodes (see experimental and supporting information sections for details). More  
354 reliable data can be obtained from the 100% charged, 50% discharged and 100%  
355 discharged electrodes, where  $\text{Li}_2\text{CO}_3$  is absent from the surfaces. Even for these  
356 electrodes, there is a discrepancy observed between the surface and the bulk with 23%  
357 and 12% changes, respectively, going from the fully charged electrode to the one  
358 discharged to 2.5 V. The observation is consistent with the fact that the surfaces of NMC  
359 materials usually undergoes more dramatic structural changes after extended cycles (as  
360 discussed below).

361           There has been much debate about the possible role that oxygen plays in layered  
362 transition metal oxide redox processes during electrochemical cycling, particularly when  
363 high voltage cutoffs are used with Li-rich materials.<sup>45-47</sup> It has also been reported that  
364 oxygen anions are involved in charge compensation through reversible charge  
365 redistribution between transition metal and oxygen in spinel<sup>48</sup> and layered oxides (e.g.,  
366 NMC-333<sup>49</sup>). However, for the NMC-333 material, only the TEY mode was used to  
367 investigate the oxygen K-edge in that study, which only provided information about  
368 surface oxygen. In studies reported by Yoon et al., both surface (TEY) and bulk (FY)  
369 oxygen activities were investigated for  $\text{LiNi}_{0.5}\text{Mn}_{0.5}\text{O}_2$ ,<sup>50</sup> NMC-333,<sup>51</sup>  $\text{LiCoO}_2$ ,<sup>52</sup> NCA,<sup>30</sup>  
370 and  $\text{LiNiO}_2$ <sup>27</sup> materials. The conclusions in these studies were that oxygen anions  
371 participated more significantly in the charge compensation (through core-hole  
372 distribution) when Co cations were present, and the surface and bulk oxygen activities  
373 became more distinct in high Ni content layered materials than in NMCs with lower Ni  
374 content.

375           To investigate the effect of cycling on these phenomena, STEM-EELS and soft  
376 XAS to investigate the structural transformation of NMC-622 materials after an extended  
377 number of cycles between 2.5-4.7 V was carried out. First, a series of EELS spectra  
378 (Figure 7) were collected as a function of distance from the surface to the bulk of an  
379 NMC-622 particle extracted from an electrode cycled 50 times and stopped at 2.5V. In all  
380 three transition metals, there were consistent shifts of  $L_3$  peaks towards higher energies as  
381 the EELS scanning moved from the surface into the bulk. Conversely, O K-edge peaks  
382 shifted to lower energies from the surface to the bulk because of increased TM3d-O2p  
383 unoccupied states in the bulk. In addition, the O pre-edge features associated with TM3d-

384 O2p hybridization became stronger along the same scanning direction (Figure 7b). These  
385 collectively show that there was a significant buildup of reduced transition metals at the  
386 surfaces of the intensively cycled NMC particles. The STEM image (Figure 7d) shows  
387 that in the surface region, the lithium channels were occupied by transition metals,  
388 consistent with a transition from a layered structure to a rock-salt structure, although the  
389 transition was not as complete as seen for NMC-442 in previous studies.<sup>17,18,53</sup> Figure 7e  
390 clearly shows that the bulk retains the original layered structure with open Li channels.  
391 Ensemble-averaged soft XAS was also used to complement the observations made by  
392 STEM-EELS. As shown in Figure 7c, Mn, Co and Ni all underwent substantial reduction  
393 upon intensive cycling. Moreover, all three transition metals were more reduced on the  
394 surface (TEY) than in the bulk (FY). The oxygen K-edge XAS has lower integrated peak  
395 intensity after 50 cycles than after 1 cycle. This phenomenon is more pronounced on the  
396 surface (green curve in Figure 7c), which is consistent with the observed surface  
397 reconstruction, and suggests that the process may continue to occur even after numerous  
398 cycles.

399 Clearly, steps to decrease the reactivity of surface oxygen are necessary to  
400 improve the electrochemical performance of Ni-rich NMCs, particularly if the goal is to  
401 cycle to higher potentials to access higher practical capacities. To this end, certain  
402 strategies, such as partial Ti substitution<sup>7-9,54</sup> and coatings,<sup>55</sup> as well as the use of  
403 electrolyte additives<sup>56</sup> should prove useful.

## 404 **Conclusions**

405 In pristine NMC-622, Ni has an average valence state higher than 2+, while Mn is  
406 tetravalent and cobalt is trivalent. A thin layer of lithium carbonate is present on particle

407 surfaces, which decomposes during charge to high voltages. *In operando* XRD on NMC-  
408 622 electrodes undergoing charge to 4.7V and discharge to 2.5V show that the bulk  
409 structural changes are highly reversible, with an overall volume change of 4% when  
410 charged to 4.7V. Soft XAS studies indicate that both nickel and cobalt undergo redox  
411 during delithiation and lithiation processes, but that Ni in the bulk behaves differently  
412 from that on particle surfaces. A rigorous and detailed analysis of the oxygen K-edge  
413 spectra indicates the surface oxygen has higher reactivity than the bulk. These two  
414 observations taken together indicate that there is more charge compensation on oxygen  
415 on particle surfaces than in the bulk. This is a driving force for surface reconstruction and  
416 the formation of surface films (CEI) that increase cell impedance and lead to capacity  
417 fading. Surface reconstruction on NMC-622 is observed after one cycle and becomes  
418 more apparent after long cycling. Our study also highlights the importance of combining  
419 high spatial resolution STEM-EELS and ensemble-averaged XAS, with improved  
420 statistics, to eliminate the discrepant conclusion of chemical environment.

421

## 422 **Acknowledgments**

423 This work was supported by the Assistant Secretary for Energy Efficiency and  
424 Renewable Energy, Office of Vehicle Technologies of the U.S. Department of Energy  
425 under Contract No. DE-AC02-05CH11231. This research used resources of the Center  
426 for Functional Nanomaterials, which is a U.S. DOE Office of Science Facility, at  
427 Brookhaven National Laboratory under Contract No. DE-SC0012704. The synchrotron  
428 X-ray portions of this research were carried out at the Stanford Synchrotron Radiation  
429 Lightsource, a Directorate of SLAC National Accelerator Laboratory and an Office of

430 Science User Facility operated for the U.S. Department of Energy Office of Science by  
431 Stanford University. Use of the Stanford Synchrotron Radiation Lightsource, SLAC  
432 National Accelerator Laboratory, is supported by the U.S. Department of Energy, Office  
433 of Science, Office of Basic Energy Sciences under Contract No. DE-AC02-76SF00515.  
434 F.L. gratefully acknowledges Virginia Tech Department of Chemistry startup funds. C.T.  
435 would like to acknowledge Dr. Yanbao Fu from Lawrence Berkeley National Lab and  
436 Dr. Douglas Van Campen from SLAC for their help with the experiments.

437 This document was prepared as an account of work sponsored by the United States  
438 Government. While this document is believed to contain correct information, neither the  
439 United States Government nor any agency thereof, nor the Regents of the University of  
440 California, nor any of their employees, makes any warranty, express or implied, or  
441 assumes any legal responsibility for the accuracy, completeness, or usefulness of any  
442 information, apparatus, product, or process disclosed, or represents that its use would not  
443 infringe privately owned rights. Reference herein to any specific commercial product,  
444 process, or service by its trade name, trademark, manufacturer, or otherwise, does not  
445 necessarily constitute or imply its endorsement, recommendation, or favoring by the  
446 United States Government or any agency thereof, or the Regents of the University of  
447 California. The views and opinions of authors expressed herein do not necessarily state or  
448 reflect those of the United States Government or any agency thereof or the Regents of the  
449 University of California.

#### 450 **Additional Information**

451 Supplementary information is available on-line.

452

453

454

455 **References**

- 456 1. J. Xu, F. Lin, M. M. Doeff, and W. Tong, *J. Mater. Chem. A*, **5**, 874–901 (2017)
- 457 2. W. Liu, P. Oh, X. Liu, M.-J. Lee, W. Cho, S. Chae, Y. Kim and J. Cho, *Angew. Chem.*  
458 *Int. Ed. Engl.*, **54**, 4440–57 (2015)
- 459 3. B. Xu, D. Qian, Z. Wang, and Y. S. Meng, *Mater. Sci. Eng. R Reports*, **73**, 51–65  
460 (2012).
- 461 4. N. Nitta, F. Wu, J. T. Lee, and G. Yushin, *Mater. Today*, **18**, 252–264 (2015)
- 462 5. A. Manthiram, B. Song, and W. Li, *Energy Storage Mater.*, **6**, 125–139 (2017)
- 463 6. H.-J. Noh, S. Youn, C. S. Yoon, and Y.-K. Sun, *J. Power Sources*, **233**, 121–130  
464 (2013).
- 465 7. S. Wolff-Goodrich, F. Lin, I. M. Markus, D. Nordlund, H. L. Xin, M. Asta and M. M.  
466 Doeff, *Phys. Chem. Chem. Phys.*, **17**, 21778–21781 (2015)
- 467 8. K. C. Kam and M. M. Doeff, *J. Mater. Chem.*, **21**, 9991 (2011)
- 468 9. K. C. Kam, A. Mehta, J. T. Heron, and M. M. Doeff, *J. Electrochem. Soc.*, **159**,  
469 A1383–A1392 (2012)
- 470 10. F. Schipper, M. Dixit, D. Kovacheva, M. Talianker, O. Haik, J. Grinblat, E. M.  
471 Erickson, C. Ghanty, D. T. Major, B. Markovsky and D. Aurbach, *J. Mater. Chem. A*, **4**,  
472 16073–16084 (2016)
- 473 11. F. Lin, D. Nordlund, Y. Li, M. K. Quan, L. Cheng, T.-C. Weng, Y. Liu, H. L. Xin and  
474 M. M. Doeff, *Nat. Energy*, **1**, 15004 (2016)
- 475 12. Y. Cho, P. Oh, and J. Cho, *Nano Lett.*, **13**, 1145–1152 (2013)
- 476 13. Y.-K. Sun, S.-T. Myung, B.-C. Park, J. Prakash, I. Belharouak and K. Amine, *Nat.*  
477 *Mater.*, **8**, 320–324 (2009)

- 478 14. I. H. Son, J. H. Park, S. Kwon, J. Mun, and J. W. Choi, *Chem. Mater.*, **27**, 7370–7379  
479 (2015)
- 480 15. J. Li, L. E. Downie, L. Ma, W. Qiu, and J. R. Dahn, *J. Electrochem. Soc.*, **162**, 1401–  
481 1408 (2015).
- 482 16. X. Zhao, Q.-C. Zhuang, C. Wu, K. Wu, J.-M. Xu, M.-Y. Zhang and X.-L. Sun, *J.*  
483 *Electrochem. Soc.*, **162**, A2770–A2779 (2015)
- 484 17. F. Lin, D. Nordlund, I. M. Markus, T.-C. Weng, H. L. Xin and M. M. Doeff, *Energy*  
485 *Environ. Sci.*, **7**, 3077 (2014)
- 486 18. F. Lin, I. M. Markus, D. Nordlund, T.-C. Weng, M. D. Asta, H. L. Xin and M. M.  
487 Doeff, *Nat. Commun.*, **5**, 3529 (2014)
- 488 19. S.-K. Jung, H. Gwon, J. Hong, K.-Y. Park, D.-H. Seo, H. Kim, J. Hyun, W. Yang and  
489 K. Kang, *Adv. Energy Mater.*, **4**, 1300787 (2014)
- 490 20. J. Li, H. Liu, J. Xia, A. R. Cameron, M. Nie, G. A. Botton and J. R. Dahn, *J.*  
491 *Electrochem. Soc.*, **164**, A655–A665 (2017)
- 492 21. J. Xu, E. Hu, D. Nordlund, A. Mehta, S. N. Ehrlich, X.-Q. Yang and W. Tong, *ACS*  
493 *Appl. Mater. Interfaces*, **8**, 31677–31683 (2016)
- 494 22. W.-S. Yoon, K. Y. Chung, J. McBreen, and X.-Q. Yang, *Electrochem. commun.*, **8**,  
495 1257–1262 (2006)
- 496 23. J. Liu, T. E. Conry, X. Song, L. Yang, M. M. Doeff and T. J. Richardson, *J. Mater.*  
497 *Chem.*, **21**, 9984–9987 (2011)
- 498 24. J. Liu, T. E. Conry, X. Song, M. M. Doeff, and T. J. Richardson, *Energy Environ.*  
499 *Sci.*, **4**, 885 (2011)
- 500 25. M. M. Doeff, G. Chen, J. Cabana, T. J. Richardson, A. Mehta, M. Shirpour, H.

501 Duncan, C. Kim, K. C. Kam and T. Conry, *J. Vis. Exp.*, e50594 (2013)

502 26. F. M. F. de Groot, J. C. Fuggle, B. T. Thole, and G. A. Sawatzky, *Phys. Rev. B*, **42**,

503 5459–5468 (1990)

504 27. W. S. Yoon, K. Y. Chung, J. McBreen, D. A. Fischer, and X.-Q. Yang, *J. Power*

505 *Sources*, **163** (2006)

506 28. F. M. F. De Groot, M. Gnom, J. C. Fuggle, J. Ghijsen, G. A. Sawatzky, H. Petersen,

507 B. Elektronenspeicherring-Gesellschaft, S. M and H. Sy, *Phys. Rev. B*, **40**, 15–1989

508 29. Y. Uchimoto, H. Sawada, and T. Yao, *J. Power Sources*, **97–98**, 326–327 (2001)

509 30. W.-S. Yoon, K. Y. Chung, J. McBreen, D. A. Fischer, and X.-Q. Yang, *J. Power*

510 *Sources*, **174**, 1015–1020 (2007)

511 31. W. S. Yoon, M. Balasubramanian, K. Y. Chung, X. Q. Yang, J. McBreen, C. P. Grey

512 and D. A. Fischer, *J. Am. Chem. Soc.*, **127**, 17479–17487 (2005).

513 32. C. S. Yoon, M. H. Choi, B.-B. Lim, E.-J. Lee, and Y.-K. Sun, *J. Electrochem. Soc.*,

514 **162**, A2483–A2489 (2015)

515 33. E.-J. Lee, Z. Chen, H.-J. Noh, S. C. Nam, S. Kang, D. H. Kim, K. Amine and Y.-K.

516 Sun, *Nano Lett.*, **14**, 4873–4880 (2014)

517 34. N. Kızıldağ-Yavuz, M. Herklotz, A. M. Hashem, H. M. Abuzeid, B. Schwarz, H.

518 Ehrenberg, A. Mauger and C. M. Julien, *Electrochim. Acta*, **113**, 313–321 (2013).

519 35. R. Hausbrand, G. Cherkashinin, H. Ehrenberg, M. Gröting, K. Albe, C. Hess and W.

520 Jaegermann, *Mater. Sci. Eng. B*, **192**, 3–25 (2015).

521 36. X. . Yang, X. Sun, and J. McBreen, *Electrochem. commun.*, **1**, 227–232 (1999).

522 37. D. Asakura, E. Hosono, Y. Nanba, H. Zhou, J. Okabayashi, C. Ban, P.-A. Glans, J.

523 Guo, T. Mizokawa, G. Chen, A. J. Achkar, D. G. Hawthron, T. Z. Regier and H. Wadati,



524 *AIP Adv.*, **6**, 35105 (2016).

525 38. R. Qiao, Y. Wang, P. Olalde-Velasco, H. Li, Y.-S. Hu and W. Yang, *J. Power*  
526 *Sources*, **273**, 1120–1126 (2015).

527 39. R. H. Potze, G. A. Sawatzky, and M. Abbate, *Phys. Rev. B*, **51**, 11501–11506 (1995)

528 40. H.-J. Lin, Y. Y. Chin, Z. Hu, G. J. Shu, F. C. Chou, H. Ohta, K. Yoshimura, S.  
529 Hébert, A. Maignan, A. Tanaka, L. H. Tjeng and C. T. Chen, *Phys. Rev. B*, **81**, 115138  
530 (2010)

531 41. D. P. Abraham, J. Liu, C. H. Chen, Y. E. Hyung, M. Stoll, N. Elsen, S. Maclaren, R.  
532 Twesten, R. Haasch, E. Sammann, I. Petrov, K. Amine and G. Henriksen, *J. Power*  
533 *Sources*, **119–121**, 511–516 (2003)

534 42. D. P. Abraham, R. D. Twesten, M. Balasubramanian, I. Petrov, J. Mcbreen and K.  
535 Amine, *Electrochem. commun.*, **4**, 620–625 (2002)

536 43. D. P. Abraham, R. D. Twesten, M. Balasubramanian, J. Kropf, D. Fischer, J.  
537 McBreen, I. Petrov and K. Amine, *J. Electrochem. Soc.*, **150**, A1450 (2003)

538 44. J. Suntivich, W. T. Hong, Y.-L. Lee, J. M. Rondinelli, W. Yang, J. B. Goodenough,  
539 B. Dabrowski, J. W. Freeland and Y. Shao-Horn, *J. Phys. Chem. C*, **118**, 1856–1863  
540 (2014)

541 45. K. Luo, M. R. Roberts, R. Hao, N. Guerrini, D. M. Pickup, Y.-S. Liu, K. Edström, J.  
542 Guo, A. V. Chadwick, L. C. Duda and P. G. Bruce, *Nat. Chem.*, **8**, 1–17 (2016)

543 46. R. Yuge, A. Toda, S. Kuroshima, H. Sato, T. Miyazaki, N. Tamura, M. Tabuchi and  
544 K. Nakahara, *Electrochim. Acta*, **189**, 166–174 (2016)

545 47. M. Oishi, K. Yamanaka, I. Watanabe, K. Shimoda, T. Matsunaga, H. Arai, Y. Ukyo,  
546 Y. Uchimoto, Z. Ogumi and T. Ohta, *J. Mater. Chem. A*, **4**, 9293–9302 (2016)

547 48. J. Zhou, D. Hong, J. Wang, Y. Hu, X. Xie and H. Fang, *Phys. Chem. Chem. Phys.*,  
548 **16**, 13838–13842 (2014)

549 49. M. G. Kim, H. J. Shin, J.-H. Kim, S.-H. Park, and Y.-K. Sun, *J. Electrochem. Soc.*,  
550 **152**, A1320 (2005)

551 50. W.-S. Yoon, M. Balasubramanian, X.-Q. Yang, Z. Fu, D. A. Fischer and J. McBreen,  
552 *J. Electrochem. Soc.*, **151**, A246 (2004)

553 51. W.-S. Yoon, Y. Paik, X.-Q. Yang, M. Balasubramanian, J. McBreen and C. P. Grey,  
554 *Electrochem. Solid-State Lett.*, **5**, A263 (2002)

555 52. W. S. Yoon, K. B. Kim, M. G. Kim, M. K. Lee, H. J. Shin, J. M. Lee, J. S. Lee and C.  
556 H. Yo, *J. Phys. Chem. B*, **106**, 2526–2532 (2002).

557 53. F. Lin, D. Nordlund, T. Pan, I. M. Markus, T.-C. Weng, H. L. Xin, M. M. Doeff and  
558 M. M. Doe, *J. Mater. Chem. A*, **2**, 19833–19840 (2014)

559 54. I. M. Markus, F. Lin, K. C. Kam, M. Asta and M. M. Doeff, *J. Phys. Chem. Lett.*, **5**,  
560 3649–3655 (2014)

561 55. X. Fang, F. Lin, D. Nordlund, M. Mecklenburg, M. Ge, J. Rong, A. Zhang, C. Shen,  
562 Y. Liu, Y. Cao, M. M. Doeff and C. Zhou, *Adv. Funct. Mater.*, **27**, 1602873 (2017)

563 56. S. R. Li, N. N. Sinha, C. H. Chen, K. Xu, and J. R. Dahn, *J. Electrochem. Soc.*, **160**,  
564 A2014–A2020 (2013)

565

566

567

568

569

570

571

572

573

574

575

576

577

578

579 **Figure Captions**

580 **Figure 1.** (a) SEM images of secondary particles and (inset) primary particles of NMC-  
581 622 prepared by spray pyrolysis. (b) XRD pattern with Rietveld refinement. (c) High-  
582 resolution Z-contrast ADF-STEM image of NMC-622 primary particle. (d) EELS survey  
583 image and (e) EELS spectra integrated from surface to bulk (red arrow direction) of the  
584 area in the green box in Figure 1 (d).

585

586 **Figure 2.** Soft XAS spectra of pristine NMC-622 (a) Mn L-edge, (b) Co L-edge and (c)  
587 Ni L-edge (orange dashed line is for NMC-333 material used as a Ni<sup>2+</sup> reference) and (d)  
588 O K-edge using AEY (black), TEY (red) and FY (blue) modes. (e) Soft XAS O K-edge  
589 spectra of different standard samples (blue for NiO, green for Li<sub>2</sub>CO<sub>3</sub>, pink for MnO<sub>2</sub>,  
590 brown for LiCoO<sub>2</sub> and orange for LiNiO<sub>2</sub>) and pristine NMC-622 (black circled curve for  
591 TEY/surface and red circled curve for FY/bulk). Numbers 1, 2, 3 and 4 labeled in d and e  
592 are identical.

593

594 **Figure 3.** a) *In situ* synchrotron XRD patterns of the first charge and discharge of an  
595 NMC-622 cathode between 2.5 V and 4.7 V at a C/10 (1C=270mAh/g) rate. Reflections  
596 are indexed. The blue asterisks represent the aluminum current collector and the green #  
597 signs are associated with polymer components (i.e., separator, kapton tape and polyester  
598 pouch material). Cell potentials are given at the right of the figure. (b) Lattice constants  
599 evolution (black and red circles represent lattice constant c while pink and green circles  
600 represent lattice constant a for H1 and H2 phase during charge; Bright and dark blue  
601 triangles are lattice constant c and a during discharge) and (c) unit cell volume change  
602 (black squares for H1 phase and red spheres for H2 phase during charge; blue triangles  
603 for volume change during discharge) of NMC-622 as a function of time during the first  
604 cycle.

605

606 **Figure 4.** (a) Mn, Co and Ni L<sub>3</sub>-edge soft XAS spectra of electrodes at various SOCs in  
607 TEY (solid lines) and FY (dashed lines) modes and (b) the corresponding voltage profile  
608 of the initial cycle. (c) Absolute peak energy shifting of Co L<sub>3</sub>-edge and (d) relative  
609 intensity ratio between Ni L<sub>3</sub> high energy peak (peak B) to low energy peak (peak A) (Ni  
610 L<sub>3 high</sub>/L<sub>3 low</sub>) at different SOCs in TEY (open squares) and FY (solid spheres) modes.  
611 Different colors represent various SOCs in a-d: black-pristine electrode; red-50%  
612 charged; blue-100% charged (4.7 V); pink-50% discharged; green-100% discharged (2.5  
613 V).

614

615 **Figure 5.** O-K edge soft XAS spectra of electrodes at various SOC's in (a) TEY and (b)  
616 FY modes. Region #1 (green shaded area) includes pre-edge features associated with  
617 TM3d-O2p hybridization states and region #2 (pink shaded area) a fingerprint of surface  
618 Li<sub>2</sub>CO<sub>3</sub>. Integrated peak areas (region 1 only) of TEY and FY data are shown in (c) and  
619 (d), respectively. Different colors represent various SOC's: black-pristine electrode; red-  
620 50% charged; blue-100% charged (4.7 V); pink-50% discharged; green-100% discharged  
621 (2.5 V). Orange error bars in (c) and (d) are based on a correction by removing surface  
622 Li<sub>2</sub>CO<sub>3</sub> layer contribution to the post-edge normalization; violet error bars are associated  
623 with “self-absorption effect” correction under FY mode. The dashed gray lines are added  
624 for visual enhancement.

625

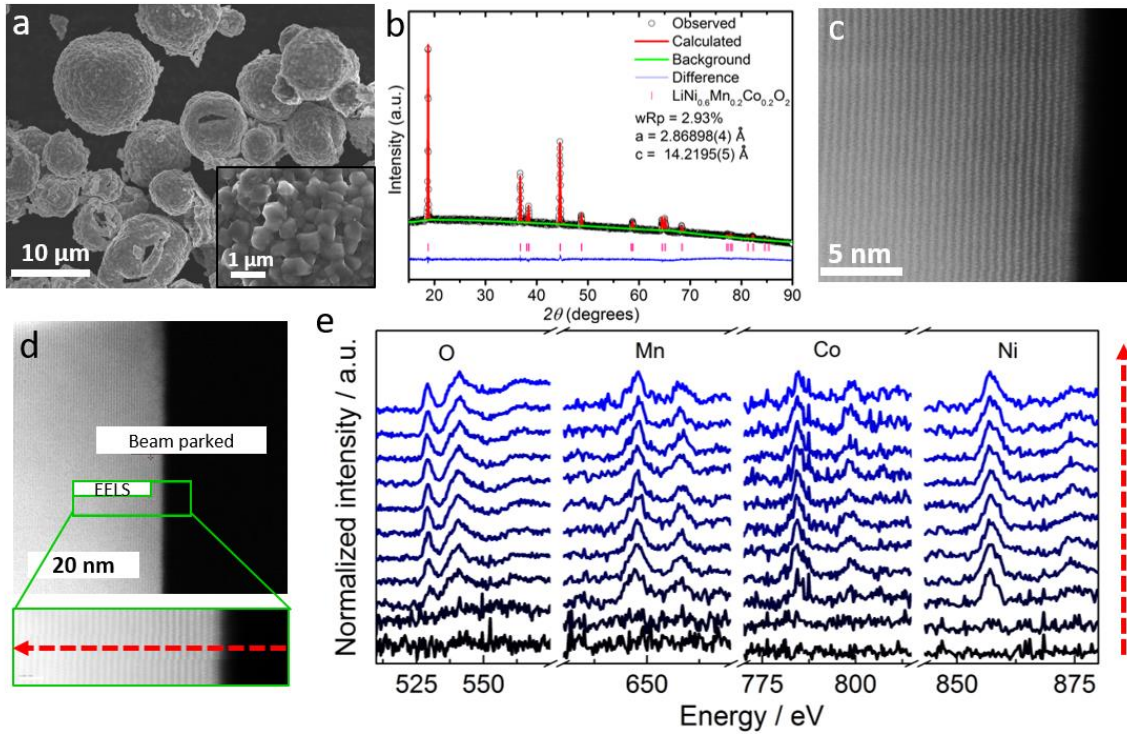
626 **Figure 6.** Comparative integrated relative peak areas of region #1 in a) TEY and b) FY  
627 modes through peak fitting from the data shown in Figure 5 for electrodes at various  
628 states-of-charge. Orange error bars are based on a correction by removing surface Li<sub>2</sub>CO<sub>3</sub>  
629 layer contribution to the post-edge normalization; violet error bars are associated with  
630 “self-absorption effect” correction under FY mode. The dashed gray lines are added for  
631 visual enhancement.

632

633 **Figure 7.** a) EELS spectra of O, Mn, Co and Ni integrated from the surface to the bulk of  
634 primary particle that was cycled to 4.7 V 50 times and stopped at 2.5V. The distance  
635 from the surface to the bulk is 12 nm. The red dashed line corresponds to the peak energy  
636 on the surface, while the green dashed line corresponds to the peak energy in the bulk. (b)  
637 Integrated peak intensity of O pre-edge in the lower energy region as a function of EELS

638 scanning depth. The red arrow shows an increasing integrated intensity (increasing  
639 number of unoccupied states) from the surface to the bulk. (c) Soft XAS spectra of O K-  
640 edge, Mn, Co and Ni L<sub>3</sub>-edge of electrodes collected after 1 cycle and 50 cycles and  
641 stopped in the discharged state. Black curve- 1cycle TEY mode; red curve-1 cycle FY  
642 mode; green curve- 50 cycles TEY mode; blue curve-50 cycles FY mode. Representative  
643 STEM images of NMC-622 primary particles after 50 cycles (d) on the surface and (e) in  
644 the bulk (the white and green arrows indicate the Li channels).

645



646

647

648

649

650

651

652

653

654

655

656

657

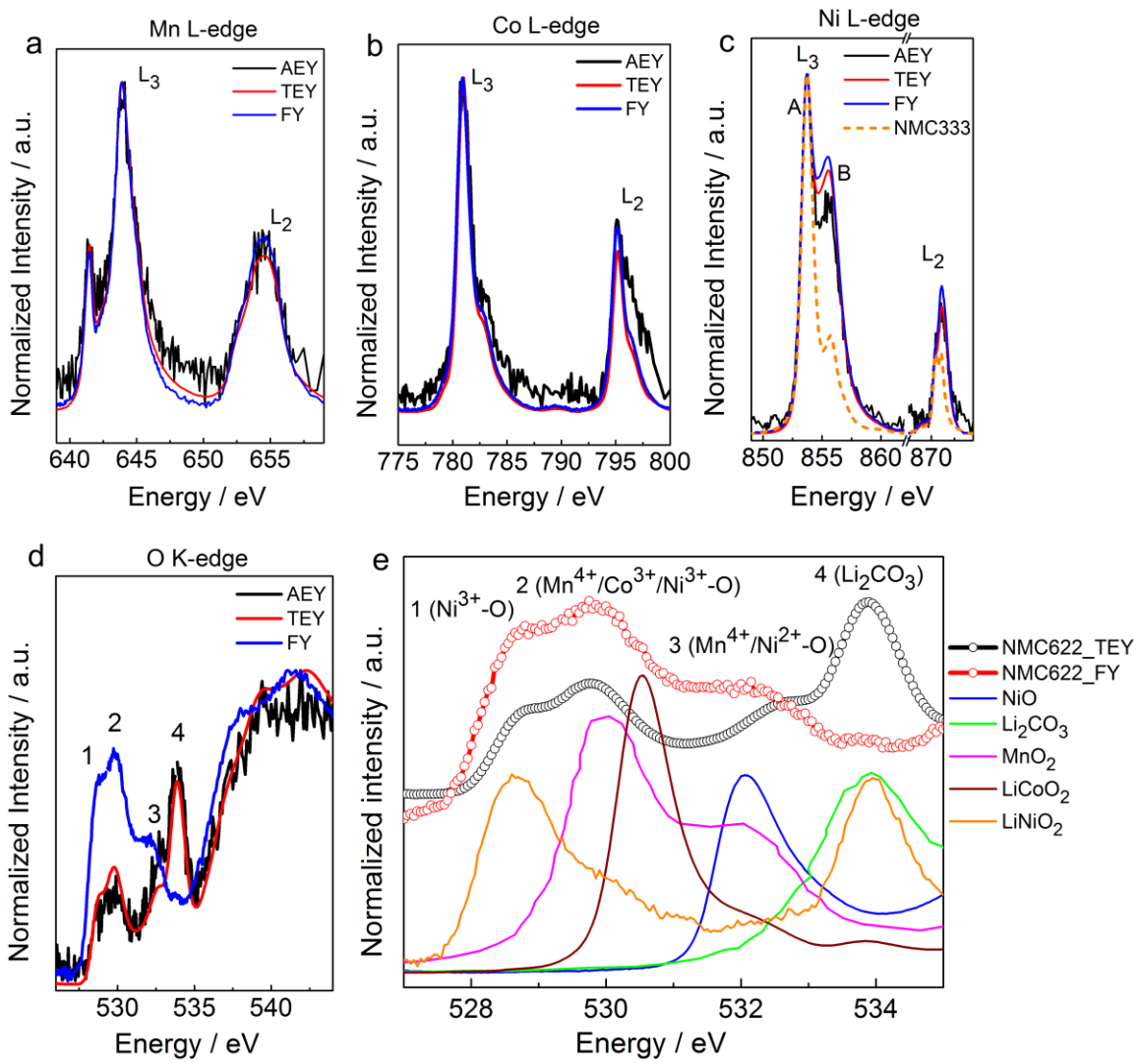
658

659

**Figure 1**

660

661



662

663

664

665

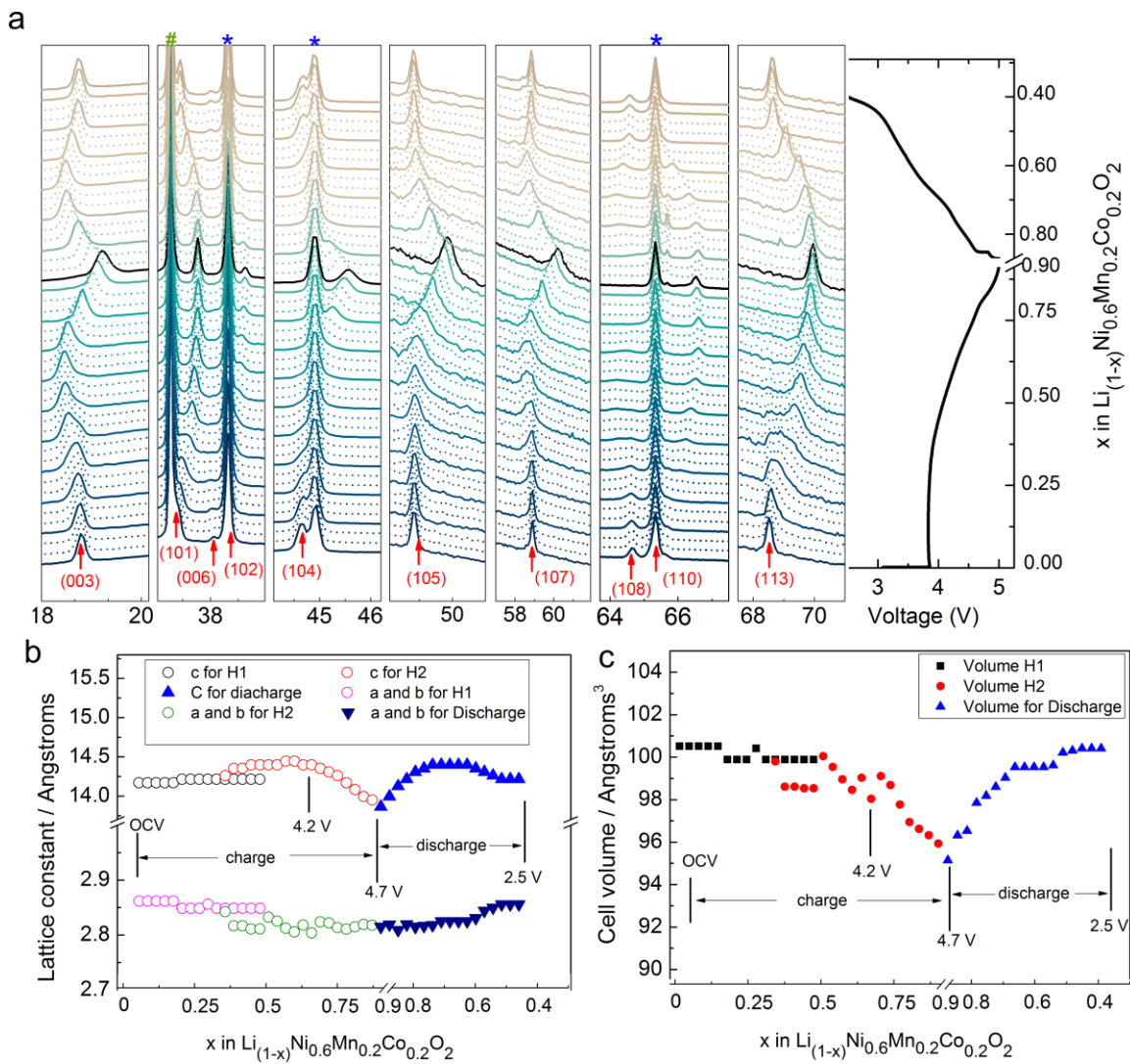
666

667

668

Figure 2





669

670

671

672

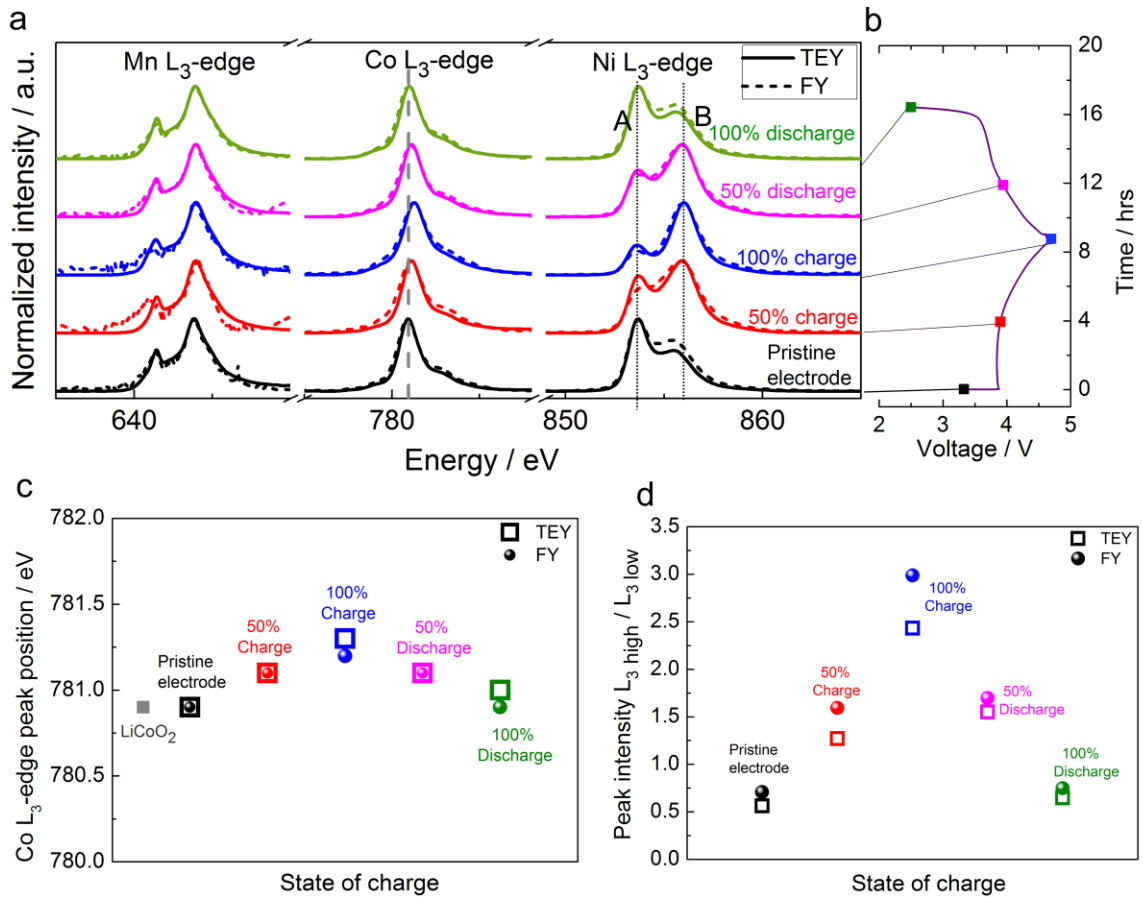
673

674

675

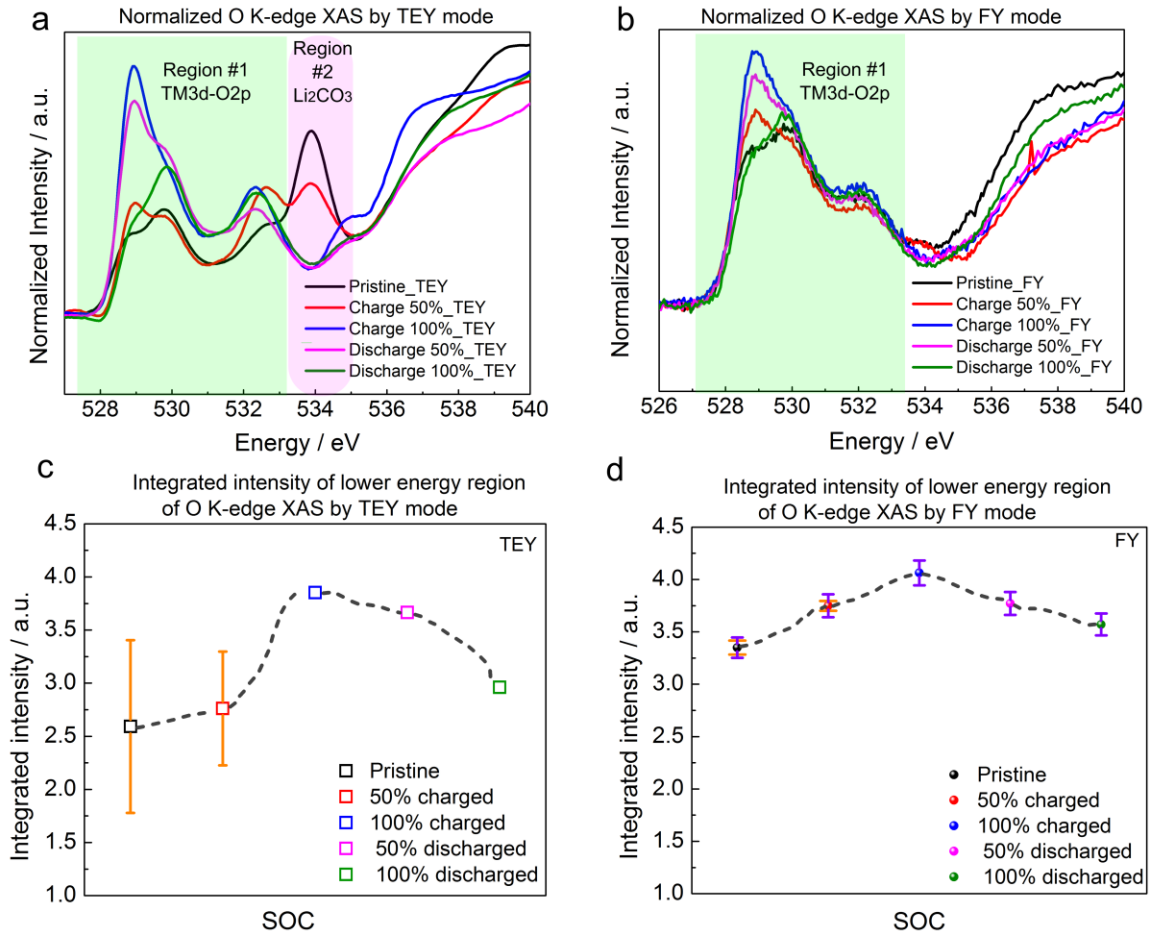
676

**Figure 3**



677  
 678  
 679  
 680  
 681  
 682  
 683  
 684  
 685  
 686  
 687  
 688

Figure 4



689

690

691

692

693

694

695

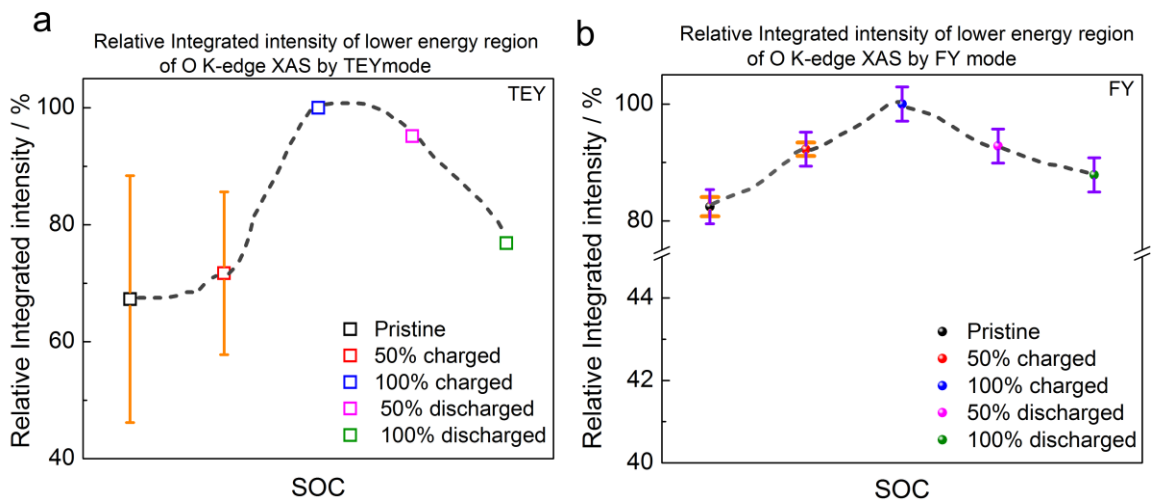
696

697

698

699

**Figure 5**



700

701

702

703

704

705

706

707

708

709

710

711

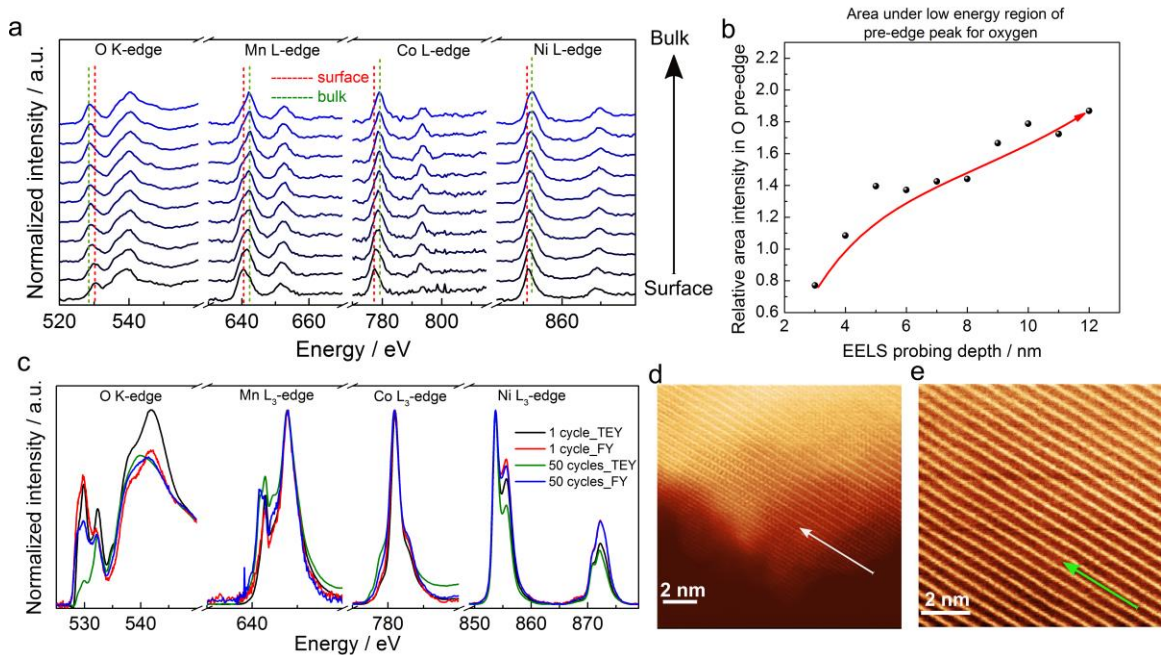
712

713

714

715

**Figure 6**



716

717

718

719

720

721

722

723

724

725

726

727

728

729

730

**Figure 7.**